k-Space Decomposition-Based 3-D Imaging With Range Points Migration for Millimeter-Wave Radar

Yoshiki Akiyama, Tomoki Ohmori, and Shouhei Kidera, *Member, IEEE*

***Abstract*— In this article, we present a novel method that incorporates the range points migration (RPM) method, *k*-space decomposition-based accurate, and noise-robust range extraction filter for microwave or millimeter-wave (MMW) short-range radar using a considerably lower fractional bandwidth signal. The advantage for higher angular resolution in higher frequency systems, such as MMW radar, has been implemented to the incoherent-based RPM method, using the simple 1-D or 2-D Fourier transform-based processing to maintain the imaging accuracy in RPM processing for both the range and the angular directions. As an additional advantage of our method, it also offers data clustering in *k*-space, which can enhance the imaging accuracy of the RPM method. The numerical and experimental tests demonstrated that the proposed method offers numerous advantages over the Capon-based super-resolution algorithm or coherent-based imaging approaches.**

***Index Terms*— Human recognition, millimeter-wave (MMW) radar, range points (RPs) migration (RPM), 3-D radar imaging.**

I. Introduction

CURRENTLY, there is a growing demand for highly accurate 3-D imaging techniques for microwave or millimeter-wave (MMW) radars assuming short-range object detection or recognition. The advantages of these techniques are particularly manifest in optically blurred environments, such as dense fog, dusty air, or over-the-horizon or through-the-wall situations. These advantages are also significant in other applications, such as collision-avoidance systems for self-driving vehicles, robotic sensors for human detection [1], [2], and security screening for concealed weapons and explosives at stations or airports [3].

In particular, MMW radars provide a higher azimuth resolution compared with lower frequency-band radar systems. Several studies have been conducted on the applications of MMW radars, such as range and Doppler velocity estimation and 3-D imaging. There are different approaches using the aforementioned background based on confocal and coherent integration processing algorithms, such as synthetic aperture radar (SAR) [4], multidimensional beamforming [5], the Kirchhoff migration approaches [6], or range migration algorithm (RMA) [7], [8], where a higher azimuth resolution is obtained via a coherent process. However, most of the abovementioned methods incur high computational costs, especially for generating high-resolution 3-D images. In addition, they generate a speckle noise or grating lobe effect because of the coherent integration process. Recently, sparsity-driven imaging algorithms, such as the compressed sensing (CS) scheme, have been introduced to reduce the volume of the observation data without degrading the imaging quality or resolution and avoid the grating lobe effect [9], assuming a sparse array configuration. For example, it was demonstrated in [10] that a considerable reduction in the processed data volume can be accomplished using sparsity-driven change detection and reconstruction by CS. Similarly, it was shown in [11] that high-resolution 3-D volumetric imaging can be achieved using fewer antenna elements assuming a multiple-input and multiple-output sparse array. However, there are limitations in CS-based reconstruction schemes, such as much higher computational cost, comparing the beamforming-based methods [4]–[6], [8], because they are required to solve large-scale optimization problems, especially for generating 3-D images.

A method called the RPM method, which exploits the time delays observed at different sensor locations, has been developed [12] to overcome the limitations in the abovementioned traditional approaches. Especially, each time delay in RPM, the so-called RPs (defined as a set of sensor locations and measured range), is efficiently converted into a reflection point on the target boundary by a stochastic estimator with a Gaussian kernel density based upon the direction-of-arrival (DOA) estimator. A notable feature of RPM is that it can be implemented with a simple algorithm because no connection or tracking scheme is required for the RPs. It also substantially addresses the association problem between the range and the DOA in time-delay-based spatial interferometers [13], [14]. In addition, it offers significant advantages over coherent-based imaging methods, such as the ability to avoid false images due to the sidelobe or grating lobe effect caused by coherent processes, which have been demonstrated in different applications [16], [17]. In particular, the study in [17] has demonstrated that the RPM offers a highly accurate 3-D image, even for a realistic human shape target using a large aperture observation model. It should be noted that the

Manuscript received June 25, 2020; revised August 26, 2020; accepted October 4, 2020. This work was supported by JST, PRESTO, Japan, under Grant JPMJPR1771. *(Corresponding author: Shouhei Kidera.)*

Yoshiki Akiyama and Tomoki Ohmori are with the Graduate School of Informatics and Engineering, The University of Electro-Communications, Tokyo 182-8585, Japan.

Shouhei Kidera is with the Graduate School of Informatics and Engineering, The University of Electro-Communications, Tokyo 182-8585, Japan, and also with the Japan Science and Technology Agency (JST), PRESTO, Saitama 332-0012, Japan (e-mail: kidera@uec.ac.jp).

Color versions of one or more of the figures in this article are available online at http://ieeexplore.ieee.org.

Digital Object Identifier 10.1109/TGRS.2020.3029301

spatial resolution of RPM is basically determined by the range resolution. Moreover, the cooperative use of super-resolution filters (e.g., the Capon method [18] and CS filter [19]) is promising for extracting highly accurate imaging features. However, MMW radar systems offer considerably narrower fractional bandwidths (i.e., a much lower range resolution), thus making it difficult to achieve the full potential of RPM. In contrast, coherent-based methods, such as the SAR or delay and sum (DAS) methods, offer higher angular resolutions, which are determined by the center wavelength and synthetic aperture angle.

As a promising solution to overcome the drawbacks of RPM, we, herein, introduce the k-space decomposition algorithm for the preprocessing of RPM, following the basic idea proposed in [21]. In this algorithm, the data received from different antenna locations are converted into k-spaces for each range gate via the Fourier transform. Responses from multiple targets are then extracted in the k-space, which is equivalent to angular-based decomposition. The notable feature of this method is that all RPs are simultaneously clustered to each part of the target, which considerably enhances the processing speed and accuracy [14]. In addition, while traditional super-resolution algorithms, such as the Capon method, require much higher signal-to-noise (S/N) ratios, our proposed method offers a noise-robust performance through the coherent k-space decomposition process. It also enables us to take advantage of both RPM and coherent-based imaging approaches, such as the SAR, in which the spatial resolution is enhanced by higher frequency systems and the grating lobe suppression and data association feature are maintained via RPM processing.

Note that the real contribution of the proposed method is that it could avoid ambiguous responses due to sparsely sampled data in the coherent imaging scheme, and the far-field approximation (planar incident wave) error due to k-space decomposition or ambiguous response could also be avoided by using the RPM, namely, the incoherent conversion process from RP to its associated scattering center point. The results of geometrical optics (GO) approximation based on 2-D and 3-D numerical analyses and experimental validation using an X-band radar system demonstrate the superiority of the proposed method over previous accurate RPM methods, such as the Capon method [18] or the SAR-based imaging approaches, in terms of spatial resolution, accuracy, computational cost, and noise robustness.

II. Observation Model

Fig. 1 illustrates the observation model in the 2-D problem. For simplicity, a monostatic radar system is assumed, that is, a set of transmitting and receiving antennas is scanned along a straight line or arranged as a linear array along the x-axis. The location of the transmitting and receiving antennas is defined as $(X, 0)$. For each antenna location, the complex output of the range extraction filter (e.g., the matched filter or the Capon filter) is obtained as $s(X, R)$. Here, $R = ct/2$ is defined using a fast time t and the propagation velocity c in the air. Discrete observation data, referred to as RPs, $\boldsymbol{q}_i \equiv (X_i, R_i)$ are extracted from the local maxima of complex envelope, $|s(X, R)|$, with respect to R, where the subscript i denotes the index number of the RPs.

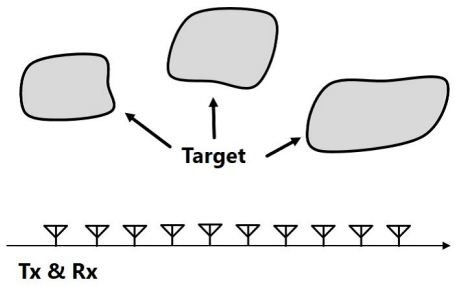

Fig. 1. Observation model in 2-D problem.

III. Conventional Radar Imaging Methods

A. Coherent Integration (Confocal) Methods

Due to a higher frequency radar system, the coherent integration-based imaging method, e.g, SAR or RMA, has a distinctive advantage that higher carrier frequencies provide higher azimuth resolutions. On the contrary, even for real aperture or synthetic aperture scenarios, these methods require dense spacing or sampling interval of observation points to avoid false images due to the grating lobe. This spacing or sampling interval must be less than half of the carrier wavelength, namely, the Nyquist criteria should be satisfied. In MMW radar systems, this limitation is more severe because the sensor separation is in the order of millimeters; hence, they require a large number of measurement positions to obtain a high azimuth resolution, which introduces high costs and more stringent hardware requirements.

B. Incoherent RP Conversion Methods

Incoherent imaging methods are proposed to address the abovementioned difficulties, especially for exploiting the reflection time delays observed at different observation points [12], [15]. Time delays obtained by reflection responses from the target are regarded as distances from the observation point to the dominant scattering center point on the target boundary. If we reconstruct each scattering center point on a continuous target boundary at each observation point, we can accurately reconstruct the target boundary. This approach is recognized as a form of spatial interferometer or multilateration. However, traditional multilateration schemes have substantial problems of association among multiple measured ranges. In particular, if a target has many scattering centers, such as the human body, these problems become fatal, incurring many false images.

The RPM algorithm was developed as a solution to the inherent problem in traditional multilateration methods, with its effectiveness demonstrated in several observation models [13], [16], [17]. RPM also adopts a time delay conversion process (multilateration approach), that is, it accurately and incoherently converts delays, the so-called RPs, into their associated scattering centers. A notable feature of RPM is that it avoids the connecting or tracking issues of RPs that arise

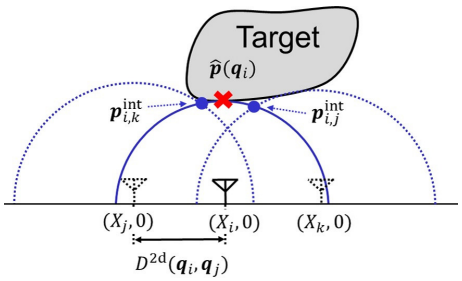

Fig. 2. Conceptual figure of the original RPM method.

from numerous objects' cases, by introducing a probabilistic assessment using the Gaussian kernel density estimator. Thus, it solves the association problem in multilateration. The methodology of RPM is briefly introduced as follows. Here, based on the GO approximation, one scattering center point on a target boundary corresponding to one RP $\boldsymbol{q}$ (named MainRP) should exist on a circle (ellipse in bistatic cases) with center X and radius R. In order to extract the scattering center point, this method calculates all the possible intersection points determined by other RPs (named SubRPs). Then, each scattering center $\hat{\boldsymbol{p}}(\boldsymbol{q}_i)$ corresponding to the MainRP is determined as

$$\hat{\boldsymbol{p}}(\boldsymbol{q}_i) = \arg\max_{\boldsymbol{p}_{i,k}^{\mathrm{int}}} \sum_{\boldsymbol{q}_j \in Q} |s(\boldsymbol{q}_j)| \exp\left[-\frac{D^{2\mathrm{d}}(\boldsymbol{q}_i, \boldsymbol{q}_j)^2}{2\sigma_D^2}\right] \times \exp\left[-\frac{\left\|\boldsymbol{p}_{i,j}^{\mathrm{int}} - \boldsymbol{p}_{i,k}^{\mathrm{int}}\right\|^2}{2\sigma_r^2}\right] \quad (1)$$

where $\boldsymbol{p}_{i,j}^{\mathrm{int}}$ denotes the intersection point of two circles determined by $\boldsymbol{q}_i$ and $\boldsymbol{q}_l$, whereas σ_r and σ_D are constants and denote correlation lengths in the Gaussian function-based weighting. Here, σ_r should be determined considering the spatial density of the accumulated intersection points, which could be roughly estimated by the aperture size and the distance from a sensor to a target. σ_D is chosen with reference to the antenna separation in the array, which should be roughly set to two or three times of sensor separations. More discussions or explanations of these parameters are described in [12]. $D^{2\mathrm{d}}(\boldsymbol{q}_i, \boldsymbol{q}_j)$ is defined as $D^{2\mathrm{d}}(\boldsymbol{q}_i, \boldsymbol{q}_j) \equiv |X_i - X_j|$, where X_i and X_j are associated with $\boldsymbol{q}_i$ and $\boldsymbol{q}_j$, respectively. $\mathcal{Q}$ denotes a set of SubRPs, which initially includes all possible RPs except MainRP as $\boldsymbol{q}_i$. It has been demonstrated in several articles that the RPM achieves accurate and high-speed imaging even in elaborate target shapes, e.g., a realistic human body [17], by being free from complicated connecting procedure of RPs. Fig. 2 shows the relationships among $\boldsymbol{p}_{i,j}^{\mathrm{int}}$, $\boldsymbol{p}_{i,k}^{\mathrm{int}}$, and $\hat{\boldsymbol{p}}(\boldsymbol{q}_i)$. As in this figure, the optimal scattering center $\hat{\boldsymbol{p}}(\boldsymbol{q}_i)$ is selected from the number of intersection points $\boldsymbol{p}_{i,j}^{\mathrm{int}}$ with the highest value of the evaluation function in the right term in (1).

Note that RPM is similar to the backprojection (BP) algorithm in SAR processing, but it is not based on a coherent process. Then, the RPM can suppress false images due to the grating or sidelobe effect, and this feature enables us to expand the aperture size with sparse sampling, which is a distinct advantage over coherent-integration-based methods. Furthermore, while coherent integration provides a higher SNR with better integration gain, compared with incoherent integration, the RPM maintains its noise-robust feature by assessing the function in (1), which denotes the reliability of each reconstructed scattered point, and then, Kidera *et al.* [12] demonstrated that RPM has the same noise–robustness level as the coherent integration scheme by exploiting the feature of (1). However, RPM loses the advantage of higher center-frequency radar systems, such as the MMW radar, because its azimuth resolution is not given by the center wavelength but rather determined by the bandwidth (i.e., the range resolution). In order to compensate for the abovementioned disadvantage, super-resolution range estimation algorithms (e.g., the Capon method [18] or CS [19]) are incorporated into RPM to provide a sufficient azimuth resolution. However, these methods require considerably high S/N ratios, higher computational complexity, and wider bandwidth, which are not always available in MMW radar systems. In order to address this limitation, the Doppler-based range decomposition has been proposed [14], where multiple RPs within a range resolution are effectively decomposed and clustered by Doppler velocity discrimination. While the effectiveness of this approach has been demonstrated in terms of accuracy and lower complexity, it makes the assumption that the target is not stationary.

IV. High-Frequency-Enhanced RPM Method

Following the discussion in the previous section, we, herein, propose a new k-space-based range decomposition method to obtain a more accurate RPs profile for the RPM imaging scheme, which is suitable for narrow-fractional-bandwidth MMW radar systems.

A. k-Space Range Decomposition

We assume that there are multiple objects and that some reflection responses are observed within the same range gate (range resolution). In order to decompose the signals that experienced interference, the proposed method converts the received complex signal via the 1-D Fourier transform as follows:

$$S(k_x, R) = \int_{X \in \Gamma} s(X, R) e^{-jk_x X} dX \quad (2)$$

where Γ denotes the aperture area and k_x denotes the wavenumber. Equation (2) is equivalent to the 1-D beamforming assuming a planar incident wave, and the DOA is linked through the relationship as $\theta = \sin^{-1}(k_x \lambda / 2\pi)$. If the DOA of each target is clearly separated in the k-space, the data associated with each target will be completely decomposed. Then, in the next step, each local maximum of $|S(k_x, R)|$ denoted as $(\tilde{k}_x, \tilde{R})$ is extracted to satisfy the following condition:

$$\left.\begin{aligned} \partial |S(k_x, R)| / \partial k_x = 0 \\ \partial |S(k_x, R)| / \partial R = 0 \end{aligned}\right\} \quad (3)$$

where the mth local maximum of $|S(k_x, R)|$ is defined as $(\tilde{k}_{x,m}, \tilde{R}_m)$, $(m = 1, \ldots, N_M)$, where N_M denotes the total number of local maxima, corresponding to the number of clusters in the RPs. Note that the proximity area around $(\tilde{k}_x, \tilde{R})$

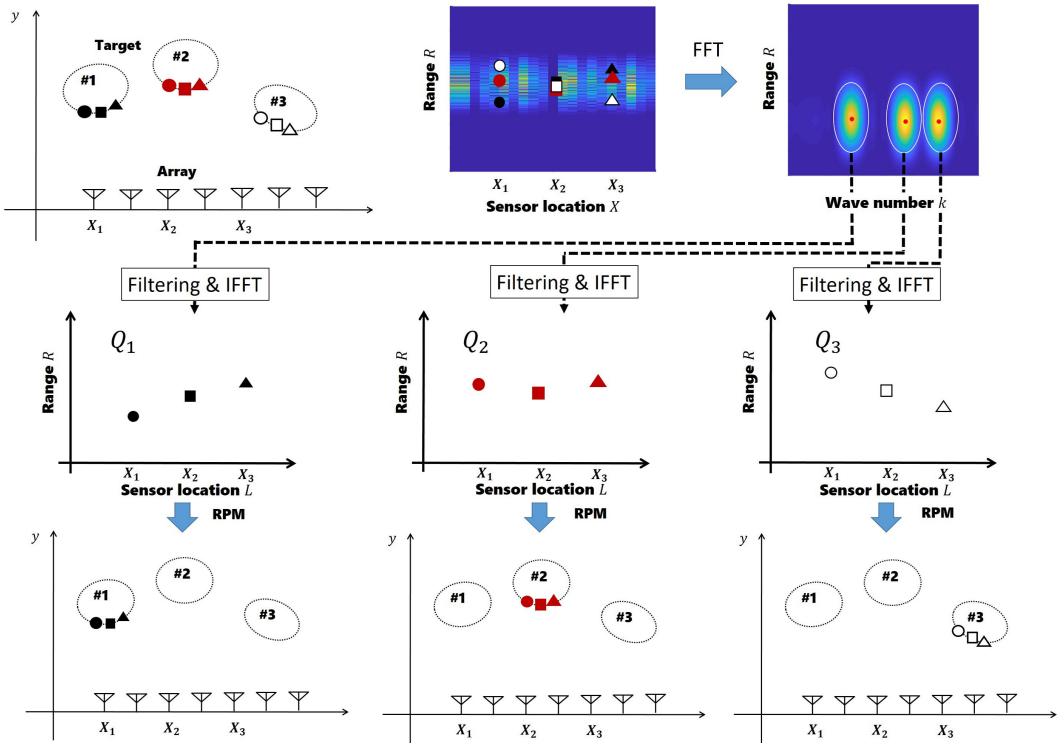

Fig. 3. Incorporation of the k-space deconvolution and the RPM method.

in the k_x-space includes most of the data generated by each target. Then, the received data are decomposed (clustered) for each $(\tilde{k}_{x,m}, \tilde{R}_m)$ as follows:

$$\tilde{s}(X, R; \tilde{k}_{x,m}, \tilde{R}_m) = \frac{1}{2\pi} \int_{k_x \in \Omega} W(k_x, R; \tilde{k}_{x,m}, \tilde{R}_m) S(k_x, R) e^{jk_x X} dk_x \quad (4)$$

where Ω is the k_x-space region and $W(k_x, R; \tilde{k}_{x,m}, \tilde{R}_m)$ denotes a spatial filter, such as raised cosine or the Gaussian filter, in the space spanning (k_x, R), with the center $(\tilde{k}_x, \tilde{R})$. Note that the filtering area of $W(k_x, R; \tilde{k}_{x,m}, \tilde{R}_m)$ should be greater than the k_x-space, which is determined by the theoretical angular resolution. Finally, the RPs for the mth clustered (decomposed) signal are extracted from the local maxima, which satisfies

$$\partial |\tilde{s}(X, R; \tilde{k}_{x,m}, \tilde{R}_m)| / \partial R = 0. \quad (5)$$

The abovementioned local maxima are newly defined as the mth clustered RPs $\boldsymbol{q}_{m,i} \equiv (X_{m,i}, R_{m,i})$, and its set is defined as

$$\mathcal{Q}_m \equiv \bigcup_{i=1}^{N_m} \boldsymbol{q}_{m,i}$$

where N_m denotes the total number of RPs included in $\mathcal{Q}_m$. Note that the abovementioned decomposition scheme is valid even if the Nyquist criterion is not satisfied, namely, a sparsely sampled array configuration, because each RP $\boldsymbol{q}_{m,i}$ is extracted from the local maxima of the complex envelope of the decomposed responses $\tilde{s}(X, R; \tilde{k}_{x,m}, \tilde{R}_m)$ in (5). This is a critical advantage of the proposed scheme.

B. Incorporation With RPM

In order to enhance the accuracy and processing speed, RPM, i.e., (1), should be applied to each cluster, whereas the scattering center generated from the ith RP included in the mth cluster as $\mathcal{Q}_m$ should be calculated as follows:

$$\hat{\boldsymbol{p}}(\boldsymbol{q}_{m,i}) = \arg\max_{\boldsymbol{p}^{\text{int}}_{m,i,l}} \sum_{\boldsymbol{q}_{m,j} \in \mathcal{Q}_m} |s(\boldsymbol{q}_{m,j})| \times \exp\left[-\frac{D^{2\text{d}}(\boldsymbol{q}_{m,i}, \boldsymbol{q}_{m,j})^2}{2\sigma_x^2} \right] \times \exp\left[-\frac{\left\| \boldsymbol{p}^{\text{int}}_{m,i,j} - \boldsymbol{p}^{\text{int}}_{m,i,l} \right\|^2}{2\sigma_r^2} \right] \quad (6)$$

where $\boldsymbol{p}^{\text{int}}_{m,i,l}$ denotes the point of intersection of the two circles determined by $\boldsymbol{q}_{m,i}$ and $\boldsymbol{q}_{m,l}$. Fig. 3 shows the schematic figure of the proposed method, where the interfered data are decomposed via the 1-D Fourier transform, and each filtered data are processed to extract the RPs belonging to the same target. Then, each set of clustered RP $\mathcal{Q}_m$ is processed by the RPM in parallel.

The proposed method can coherently decompose the range data using the DOA difference based on the simple 1-D Fourier transform, and it is then suitable for the MMW radar systems that usually have a much smaller fractional bandwidth compared with lower band ultrawideband (UWB) radar systems. The main difference from the traditional SAR or the Fourier-based RMA is that our method could avoid an ambiguous response due to a phase uncertainty by converting from RP to a scattering center. In addition, in the SAR or RMA

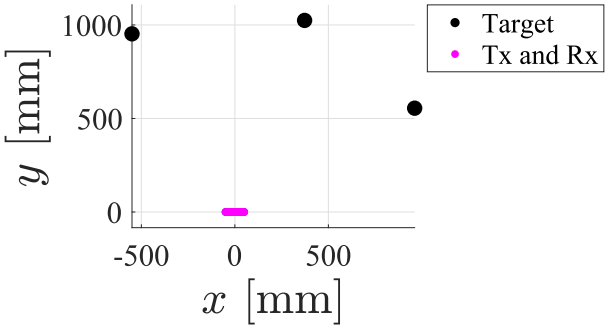

Fig. 4. 2-D numerical observation geometry.

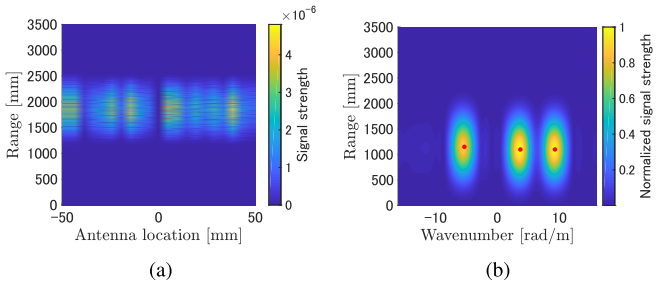

Fig. 5. (a) Received data $s(X, R)$. (b) Received data in k-space $s(k, R)$.

imaging scenario, we need to determine an appropriate region of interest (ROI), the size of which significantly affects the computational costs, especially in the full 3-D case; however, the RPM-based method does not require the prior estimation of the ROI and could reduce a redundant computational cost. Another distinctive advantage of the proposed method is that since it uses only Fourier transform analysis, its computational complexity is considerably lower than that required by the Capon or CS-based method.

V. Performance Evaluation in 2-D Problem

A. Numerical Test

1) Simulation Setup: In this section, we present a numerical test for the proposed method. We adopted GO-approximation-based data generation to deal with a large-scale problem that concerns the wavelength of the MMW radar system. The effect of multiple scattering among targets was not included, but the interference effect from the reflected signals was considered. GO is a promising forward solver based on high-frequency approximation, in which the dominant propagation path is determined by the law of reflection in optics [22]. In this case, the transmitting signal forms a pulse-modulated signal, with a center frequency of 20 GHz and a bandwidth of 0.2 GHz, which assumes the usual MMW radar system, that is, a 24-GHz-band MMW radar. In this case, the center wavelength and theoretical range resolutions are 15 and 750 mm, respectively. The set of transmitting and receiving antennas is scanned along $y = 0$, with a scanning sample interval of 5 mm, corresponding to one-third of the center wavelength (15 mm). Fig. 4 shows the observation geometry that contains three point-shaped targets. It should be noted that the maximum difference in the radial range among these three targets, that is, the line-of-sight distances, is less than 80 mm, corresponding to 0.16 times the theoretical range resolution.

2) Results in Noise-Free Case: We first tested each method in a noise-free environment to evaluate systematic errors only. Fig. 5(a) shows the received signal $s(X; R)$, after applying the matched filter and its representation in k-space, denoted as $s(X, k)$. Fig. 5(b) demonstrates that each target response in k-space (k, R) can be clearly discriminated, whereas they are hardly separated in the data space (X, R). Note that the raised cosine window is used as $W(k_x, R; \tilde{k}_{x,m}, \tilde{R}_m)$ in (4), a period of which is 417 rad/m. As a comparison study

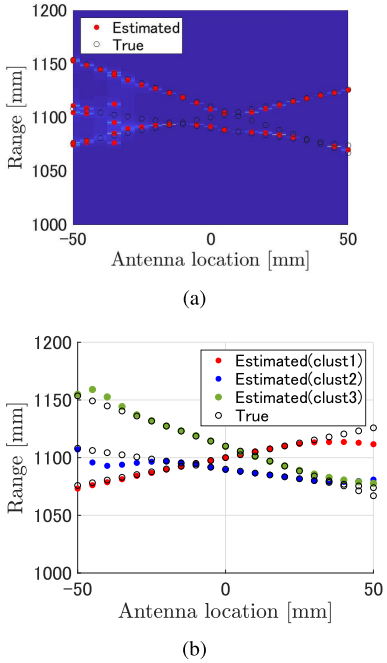

Fig. 6. Results of RP extraction in noise-free case. (a) Capon. (b) Proposed method. Color scale in (a) denotes the magnitude of the Capon response.

for the existing accurate range estimation method, Fig. 6 shows the results after applying the Capon method [23] and the proposed method. Here, we applied a simple frequency averaging scheme, in which the number of averaging is optimized in the Capon process to retain the resolution for highly correlated signal decomposition [18]. As shown in Fig. 6(a), there is a nonnegligible inaccuracy or limitation in the range extraction because the bandwidth is too narrow to provide a sufficient range resolution even while using the Capon method. In contrast, the proposed method retains a high accuracy even in this case and completely resolves the three target responses for any antenna location. It is confirmed that there is an inaccuracy in the proposed range extraction at both ends of the aperture area because the received data are not continuous between the start and end of the data along with the antenna location, whereas the DFT assumes the continuity for the start and end of the data.

For the quantitative analysis of the range estimation errors, $\mathrm{Err}_{\mathrm{range}}$ is introduced as the minimum distance between the true and estimated ranges for each RP. The cumulative probabilities to satisfy $\mathrm{Err}_{\mathrm{range}} \leq 10$ mm are 98 % (46 / 47) for the

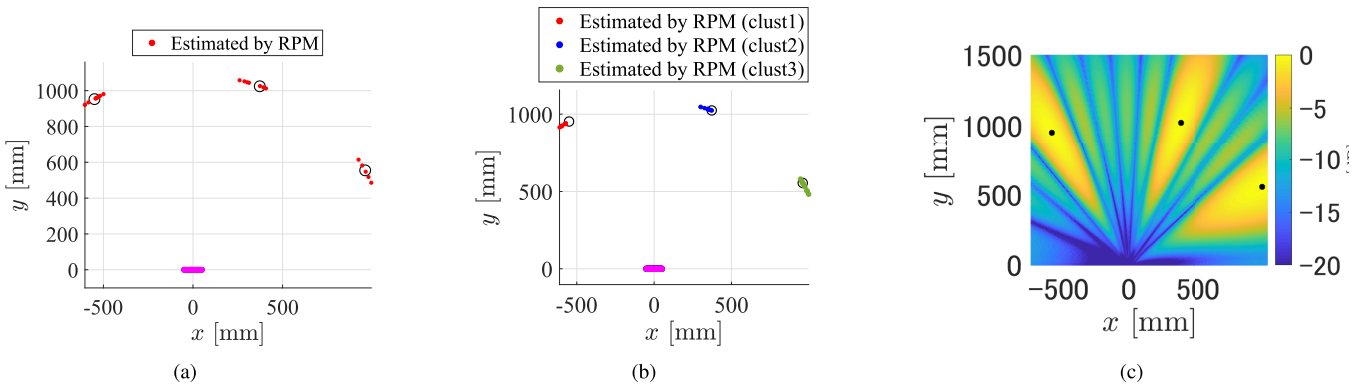

Fig. 7. Image reconstruction results. (a) RPM with Capon-based decomposition. (b) RPM with k-space decomposition (proposed). (c) SAR.

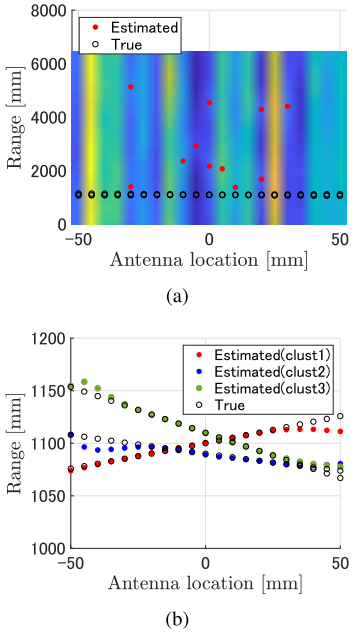

Fig. 8. Results of RP extraction at $S/N = 20$ dB. (a) Capon. (b) Proposed method. Color scale in (a) denotes the magnitude of the Capon response.

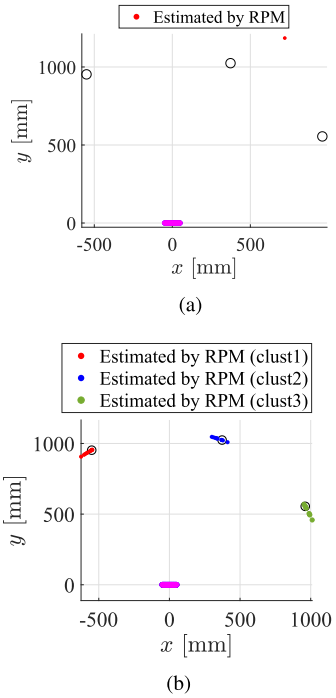

Fig. 9. Estimation results by RPM method at $S/N = 20$ dB. (a) Capon-based decomposition. (b) Wavenumber-based decomposition (proposed).

Capon method and 94 % (59/63) for the proposed method. This result indicates that the proposed method significantly increases the accuracy of the RPs using simple processing. Note that these RPs can be clustered, which enhances the accuracy and the processing speed of RPM imaging. Finally, Fig. 7 shows the RPM results for each group of RPs and the SAR image. $\sigma_x = 100$ mm and $\sigma_r = 50$ mm are set in the RPM. This figure demonstrates that the RPM images using both the Capon filter and the proposed method offer almost correct scattering center points for all three targets in the noise-free case. In addition, the SAR image could decompose the target along the azimuth direction, and its spatial resolution especially for range direction is considerably low, which hardly offers an accurate target shape or location.

3) Results in Noisy Case: In this section, we investigate the robustness of the proposed method for additive noise. The Gaussian white noises were added to the received signal as $s(X, R)$. The S/N ratio is defined as the ratio of the peak instantaneous signal power of the data to the average noise power. In this article, we first discuss a higher S/N example of an S/N ratio of 20 dB. Fig. 8 shows the results of the range extraction obtained for each method. It demonstrates that, while the proposed method retains its performance, the Capon filter could not provide good results in noisy situations. This is because the Capon filter employs a transfer function for data conversion (i.e., it is based on an inverse filter output), which is very sensitive to additive noise. Fig. 9 also shows the results of RPM imaging, in which RP extraction was performed using the Capon method and the proposed method. The figure shows that the RPs obtained using the proposed method maintain high accuracy, whereas the RPM images obtained using the Capon filter are considerably degraded compared with those obtained in a noise-free situation. Note that, while the RPM is based on the incoherent process, the k-space coherent decomposition and its filtering process considerably enhance the noise–robustness of the proposed method, which is unavailable in the original RPM. As a lower S/N situation, Fig. 10 shows the results of range extraction and RPM imaging obtained from the proposed method at S/Ns

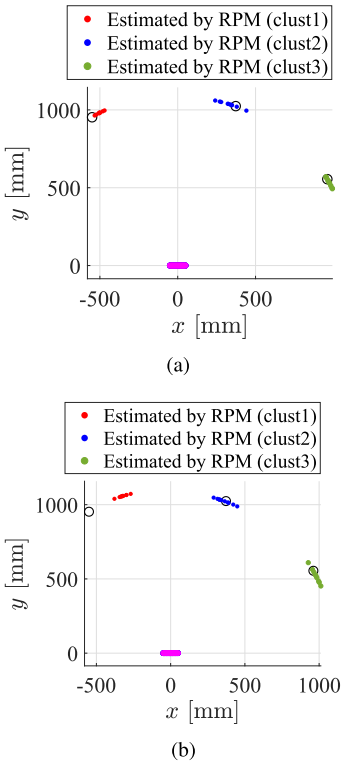

Fig. 10. Results of RPM imaging using the proposed method at (a) $S/N = 10$ and (b) 0 dB.

TABLE I

CUMULATIVE PROBABILITY FOR RANGE EXTRACTION ERRORS IN 2-D CASE

	$\mathrm{Err}_{\mathrm{Range}} \leq 10$ mm			
S/ N	∞	20 dB	10 dB	0 dB
Capon	98 % (46/47)	0 % (0/11)	0 % (0/11)	0 % (0/11)
Proposed	94 % (59/63)	95 % (60/63)	95% (61/63)	90 % (60/63)

of 10 and 0 dB. As shown in Fig. 9, it deviates slightly from the actual target positions because of strong noises, especially in the case of S/N of 0 dB, but some points still maintain its accuracy. Tables I and II show comparisons of the quantitative error for each S/N ratio for the measured ranges and RPM imaging, respectively. Note that the error in the RPM image is denoted as $\mathrm{Err}_{\mathrm{RPM}}$, which is defined as the minimum distance between the target boundary (expressed as dense discrete points) and each point estimated using the RPM method. In conclusion, the proposed method retains a certain level of accuracy over an S/N of 10 dB, which is available in the actual short-range radar scenario, as in [12] and [28].

4) Results in Sparsely Sampled Case: To reveal the advantage of the proposed method, namely, the *k*-space decomposition-based RPM imaging scheme, we added the test case, assuming the sparse array configuration or scanning sampled cases, including those obtained from the RMA method, which is known as one of the high-speed radar imaging techniques by exploiting the fast Fourier transform-based data conversion [7], [20]. Fig. 11 shows the observation model,

TABLE II

CUMULATIVE PROBABILITIES FOR RPM IMAGING ERRORS WITH DIFFERENT CRITERIA IN 2-D CASE

	$\mathrm{Err}_{\mathrm{RPM}} \leq 50$ mm			
S/ N	∞	20 dB	10 dB	0 dB
Capon	61 % (14/23)	0 % (0/1)	0 % (0/1)	0 % (0/1)
Proposed	67 % (22/33)	71 % (25/35)	50% (16/32)	35 % (11/31)
	$\mathrm{Err}_{\mathrm{RPM}} \leq 100$ mm			
S/ N	∞	20 dB	10 dB	0 dB
Capon	96 % (22/23)	0 % (0/1)	0 % (0/1)	0 % (0/1)
Proposed	100 % (33/33)	97 % (34/35)	94% (30/32)	61 % (19/31)

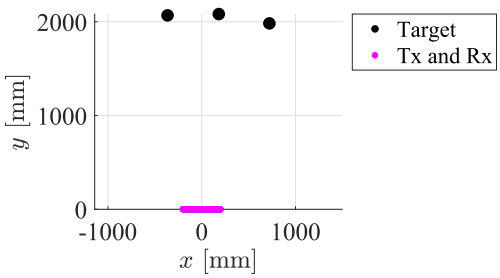

Fig. 11. 2-D numerical observation geometry, where observation points are sparsely arranged.

where the scanning sample interval is set to 20 mm, which is four times larger than that assumed in Section V-A1, and the center wavelength as 15 mm. Fig. 12(a) and (b) shows the imaging results obtained by the SAR method and the RMA method using f-k migration-based acceleration, respectively. The SAR shows some unnecessary responses along the azimuth direction due to the phase uncertainty. Furthermore, if we simply threshold the SAR images, there are many unnecessary responses due to the sidelobe or grating lobe effects. In the case of the RMA, compared with the SAR image, the image spatial resolution or magnitudes degrade due to the interpolation or filtering effect in the wavenumber domain, particularly the right-hand side of the target. Moreover, we confirmed that the RMA suffered from an ambiguous ghost response due to the coherent integration process if a target is located at a large azimuth angle, which has not occurred in the incoherent-based proposed method.

In addition, in the RMA image, the azimuth resolution and accuracy significantly depend on the selected reference range from the sensors to the targets. Consequently, if we deal with multiple targets with different ranges, its accuracy or resolution would not be guaranteed. Note that, while the RMA is much faster than the general SAR process, the pixel resolution is insufficient in this case; to obtain a more densely sampled image, the processing time could be increased rapidly. However, Fig. 12(c) shows the imaging results obtained from the proposed method, offering accurate target locations without unnecessary responses, because the conversion process from RPs to its associated scattering center is incoherent, while the

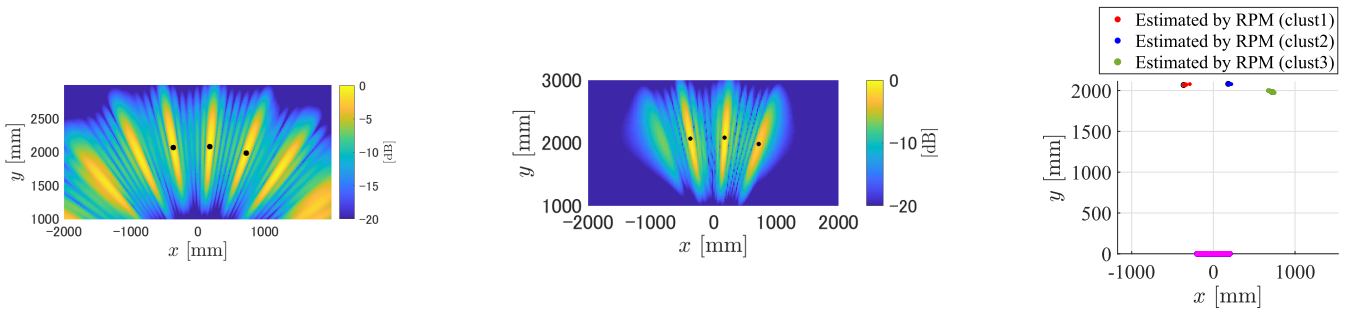

(a) (b) (c)

Fig. 12. Image reconstruction results by each method, assuming the sparsely arranged observation model. Black dots denote the actual target shape and positions. (a) SAR. (b) RMA. (c) Proposed.

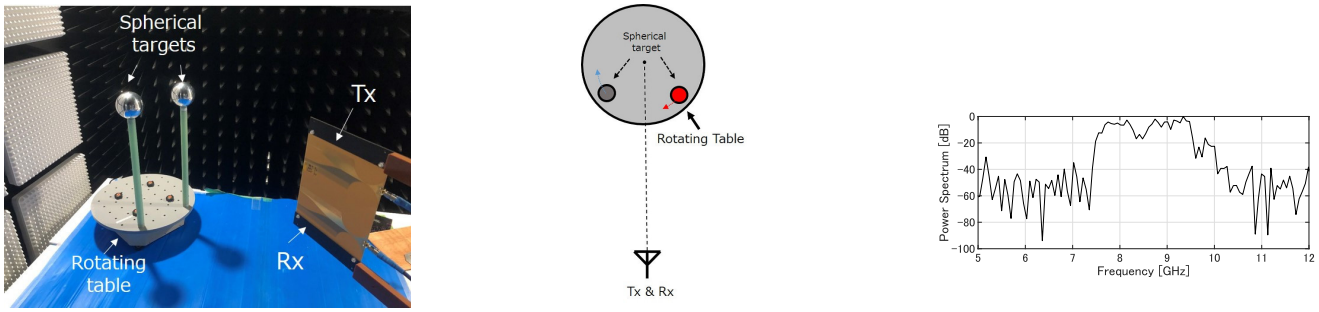

(a) (b) (c)

Fig. 13. Experimental setup including two spherical targets with rotating table and the transmitting and receiving Fermi antennas. (a) Photograph. (b) Geometrical arrangement. (c) Frequency power spectrum of reference signal.

k-space decomposition is based on coherent integration. This point is also a significant advantage of the proposed method. Note that $\sigma_x = 400$ mm and the period of the raised cosine window as $W(k_x, R; \tilde{k}_{x,m}, \tilde{R}_m)$ as 417 rad/m are set, to fit this sparse sampled case. The cumulative probabilities, for the abovementioned results in Fig. 12(c), are 87 % (55/63) for $\mathrm{Err}_{\mathrm{range}} \leq 10$ mm and 94 % (34/ 36) for $\mathrm{Err}_{\mathrm{RPM}} \leq 50$ mm, respectively, and verify that its accuracy could be maintained even in sparse sampled configuration. Furthermore, the computational time for each method is 60 s for the SAR, 25 s for the RMA, and 2 s for the proposed method, verifying the effectiveness of the proposed method regarding computational cost.

B. Experimental Test

This section presents the experimental validation for the proposed method, using X-band UWB radar equipment. Fig. 13 shows the measurement setup using a UWB impulse radar system (Sakura Tech Corp.), where the transmitting signal has a center frequency of 8.5 GHz and a 1.5-GHz 10-dB bandwidth; that is, the theoretical range resolution is 100 mm. The transmitting and receiving broadband Fermi antennas are arranged vertically, separated by 100 mm. Both the E- and H-plane 3-dB beam widths of the Fermi antennas are 40°. Two spherical targets, each with a diameter of 100 mm, are rotated by an azimuth table with an accuracy of 0.1°. In order to achieve a monostatic observation in different locations, the two targets were rotated by 20°, with 1° spacing, while the transmitting and receiving antennas were fixed. 21 sampled data points were processed in each method. The distance from the radar unit to the center of the rotation table was 978 mm and that from each target to the rotation center is 180 mm. The maximum difference from the two targets to the antenna locations is estimated to be within 60 mm. Fig. 14 shows the received data after applying a matched filter and the extracted RPs, as well as the RPM imaging results. The S/N ratio, in this case, is approximately 25 dB. $\sigma_x = 341$ mm and $\sigma_r = 10$ mm are set in the RPM. The figure shows that since the maximum difference between the two targets and the antenna locations is within the range resolution, matched filter (cross correlation)-based signal processing cannot separate the two responses, resulting in a considerable inaccuracy in the performance of the RPM imaging scheme. Fig. 15 shows the results obtained from the Capon filter, demonstrating that the Capon filter, too, could not offer a clear separation between the two target responses due to the insufficient S/N value or bandwidth, similar to the discussion presented in Section V-A3. On the contrary, Fig. 16 shows the results obtained from the k-space decomposition and the decomposed responses obtained by the proposed method. As shown in the figure, the two target responses are clearly separated in the k-space in Fig. 16(a), and each component can be reconstructed accurately via IDFT. Fig. 17 shows the performance of RPM in RP extraction and image reconstruction. It demonstrates that the proposed method considerably enhances the performance and accuracy

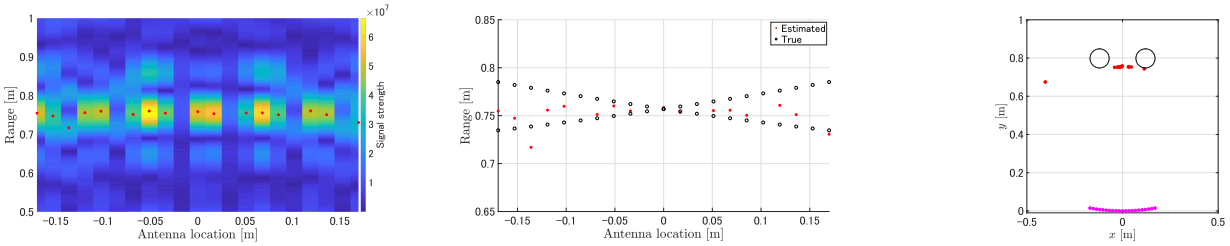

(a) (b) (c)

Fig. 14. Results obtained using the matched filter with the experimental data. (a) Response by filter. (b) True and extracted RPs. (c) Reconstructed scattering centers (red solid circles) by the RPM. Color scale in (a) denotes the magnitude of the matched filter response.

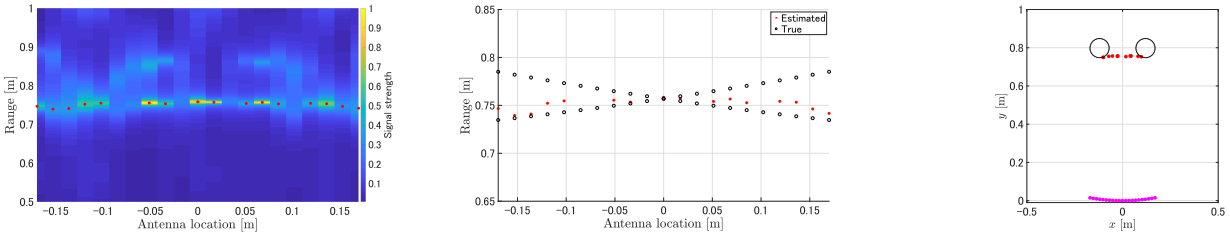

(a) (b) (c)

Fig. 15. Results in using the Capon filter with the experimental data. (a) Response by filter. (b) True and extracted RPs. (c) Reconstructed scattering centers (red solid circles) by the RPM. Color scale in (a) denotes the magnitude of the Capon response.

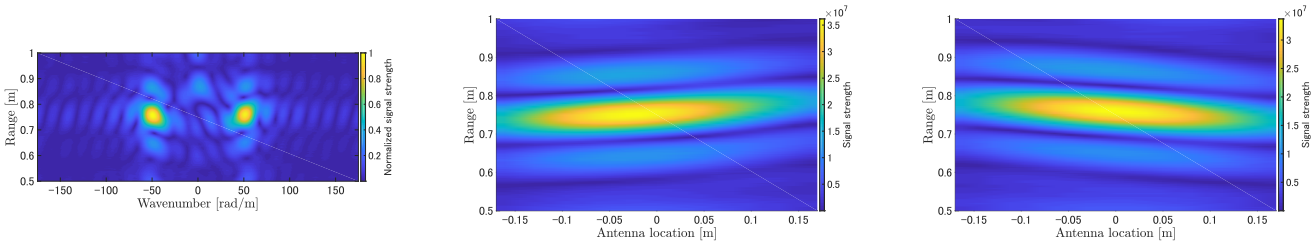

(a) (b) (c)

Fig. 16. (a) Responses in k-space with the experimental data. (b) and (c) Each decomposed response after applying k-space separation with the experimental data.

of both range extraction and RPM imaging, noting that the RPs are also correctly clustered by this method. Furthermore, Fig. 18 shows the image reconstructed by the BP-based SAR algorithm and shows that, while the target responses along azimuth direction are clearly separated, the shape of the target (spherical shape) is hardly recognized due to lower range resolution or its principle. Notably, the local maxima of SAR localize the front surface of each metallic sphere, which corresponds to the dominant reflection point. Finally, Table III summarizes the cumulative probabilities of errors in range extraction and the accuracy of RPM imaging. This table clearly denotes the superiority of the proposed method, which remarkably enhances the number of accurately reconstructed RPs and imaging points, even in experimental validations, including realistic noise.

VI. Extention to 3-D Problem

A. Methodology

This section describes the extension of the proposed method to 3-D problems. Fig. 19 shows the observation model in a 3-D problem. Similar to the 2-D problem, a monostatic radar system is assumed, but note that the proposed method would be applicable to multistatic observation in principle. Assuming a vertically arranged array or vertical plane scanning on the $y = 0$ plane, the location of the transmitting and receiving antenna is defined as $(X, 0, Z)$, and the received data for each antenna location is described as $s(X, Z, R)$. Then, the received data are converted into $k_{x,z}$-space spanned by k_x and k_z as follows:

$$S(k_x, k_z, R) = \int_{(X,Z)\in\mathbf{\Gamma}} s(X, Z, R) e^{-j(k_x X + k_z Z)} dX dZ \quad (7)$$

where Γ denotes the observation area. The decomposition in the k_x and k_z spaces is equivalent to that in the elevation and azimuth DOA domains. Next, the mth local maxima of $S(k_x, k_z, R)$ are extracted as $(\tilde{k}_{x,m}, \tilde{k}_{z,m}, \tilde{R}_m)$

$$\left.\begin{aligned} \partial|S(k_x, k_z, R)|/\partial k_x &= 0 \\ \partial|S(k_x, k_z, R)|/\partial k_z &= 0 \\ \partial|S(k_x, k_z, R)|/\partial R &= 0 \end{aligned}\right\}. \quad (8)$$

Fig. 20 shows a schematic of the extension of the proposed method to a 3-D problem.

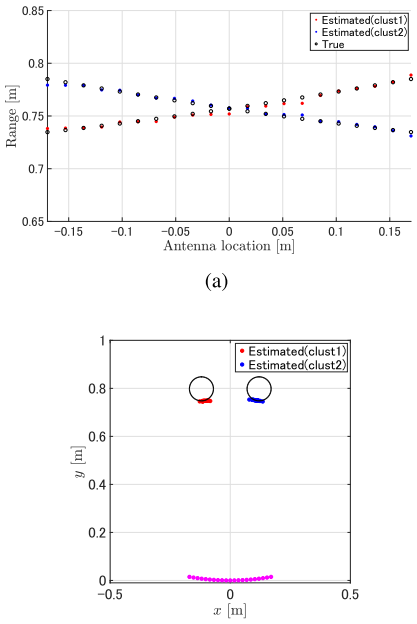

Fig. 17. Results in using the k-space decomposition (the proposed method) with the experimental data. (a) True and extracted RPs, where blue and red solid circles denote each clustered RPs. (b) Reconstruction image by the RPM, where blue and red solid circles denote scattering center processed by a group of clustered RPs in (b).

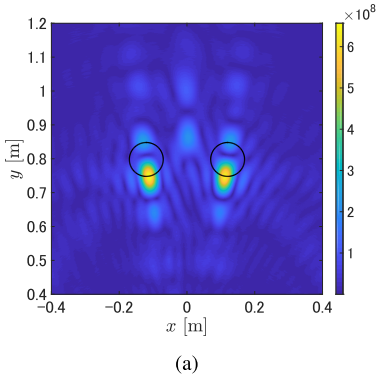

Fig. 18. Reconstructed image by the SAR algorithm.

TABLE III
CUMULATIVE PROBABILITIES FOR EACH ERROR IN EXPERIMENTAL TESTS

	$\mathrm{Err}_{\mathrm{Range}} \leq 5$ mm	$\mathrm{Err}_{\mathrm{RPM}} \leq 5$ mm
Matched filter	12.5 % (2/16)	0 % (0/16)
Capon filter	25.0 % (4/16)	18.7 % (3/16)
Proposed	71.4 % (30/42)	85.7 % (36/42)

Similar to the 2-D approach, the proximity area around $(\tilde{k}_{x,m}, \tilde{k}_{z,m}, \tilde{R}_m)$ is extracted for data decomposition and clustering. The mth clustered data are calculated via the inverse 2-D Fourier transform as follows:

$$\tilde{s}(X, Z, R; \tilde{k}_{x,m}, \tilde{k}_{z,m}, \tilde{R}_m) = \frac{1}{2\pi} \int_{(k_x,k_z)\in\boldsymbol{\Omega}} W(k_x, k_z, R; \tilde{k}_{x,m}, \tilde{k}_{z,m}, \tilde{R}_m) \times S(k_x, k_z, R) e^{j(k_x X + k_z Z)} dk_x dk_z \quad (9)$$

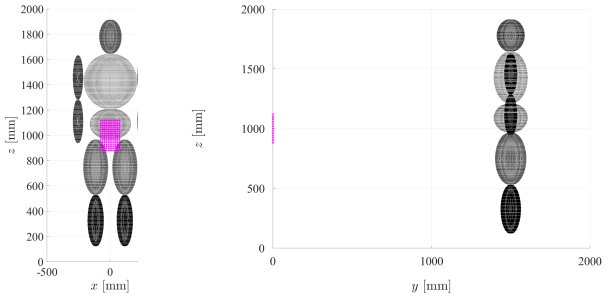

Fig. 19. Observation model in 3-D problem, assuming simplified human body target. Purple dots denote the 2-D array location.

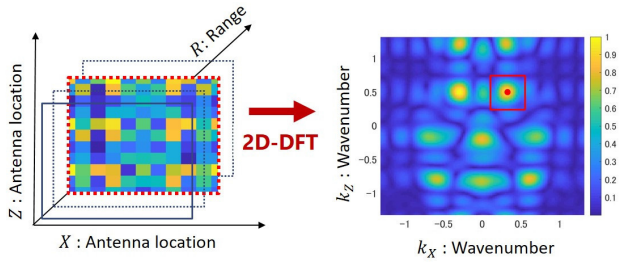

Fig. 20. 2-D k-space decomposition in the 3-D model.

where $W(k_x, k_z, R; \tilde{k}_{x,m}, \tilde{k}_{z,m}, \tilde{R}_m)$ denotes the window function as for the 2-D k_x and k_z space, not for R, with the center $(\tilde{k}_{x,m}, \tilde{k}_{z,m}, \tilde{R}_m)$. For each cluster, the RPs are extracted from the local maxima of $|\tilde{s}(X, Z, R; \tilde{k}_{x,m}, \tilde{k}_{z,m}, \tilde{R}_m)|$, Finally, RPM for the 3-D version is applied to each cluster to extract the scattering center corresponding to the RP $\boldsymbol{q}_{m,i}$ as follows:

$$\hat{\boldsymbol{p}}(\boldsymbol{q}_{m,i}) = \underset{\boldsymbol{p}^{\mathrm{int}}_{m,i,l,n}\in\mathcal{P}_{m,i}}{\arg\max} \sum_{\boldsymbol{q}_{m,j},\boldsymbol{q}_{m,k}\in\mathcal{Q}_m} g(\boldsymbol{q}_{m,i}; \boldsymbol{q}_{m,j}, \boldsymbol{q}_{m,k}) \times \exp\left[-\frac{\left\|\boldsymbol{p}^{\mathrm{int}}_{m,i,j,k} - \boldsymbol{p}^{\mathrm{int}}_{m,i,l,n}\right\|^2}{2\sigma_r^2}\right] \quad (10)$$

where $\boldsymbol{p}^{\mathrm{int}}_{m,i,l,n}$ denotes the intersection point of the spheres generated by $\boldsymbol{q}_{m,i}$, $\boldsymbol{q}_{m,l}$, and $\boldsymbol{q}_{m,n}$, $\mathcal{P}_{m,i}$ is a set, including the those intersection points. $g(\boldsymbol{q}_{m,i}; \boldsymbol{q}_{m,j}, \boldsymbol{q}_{m,k})$ is defined as

$$g(\boldsymbol{q}_{m,i}; \boldsymbol{q}_{m,j}, \boldsymbol{q}_{m,k}) = |s(\boldsymbol{q}_{m,j})| \exp\left[-\frac{D^{3\mathrm{d}}(\boldsymbol{q}_{m,i}; \boldsymbol{q}_{m,j})^2}{2\sigma_D^2}\right] + |s(\boldsymbol{q}_{m,k})| \exp\left[-\frac{D^{3\mathrm{d}}(\boldsymbol{q}_{m,i}; \boldsymbol{q}_{m,k})^2}{2\sigma_D^2}\right] \quad (11)$$

where $D^{3\mathrm{d}}(\boldsymbol{q}_{m,i}; \boldsymbol{q}_{m,j})$ denotes the 3-D Euclidean distance between the antenna locations, denoted by $\boldsymbol{q}_{m,i}$ and $\boldsymbol{q}_{m,j}$. Note that the abovementioned process can be implemented by a 2-D fast Fourier transform (FFT) algorithm.

B. Numerical Simulation Test

1) Simulation Model: In this section, we present the range extraction and imaging performances for the 3-D problem.

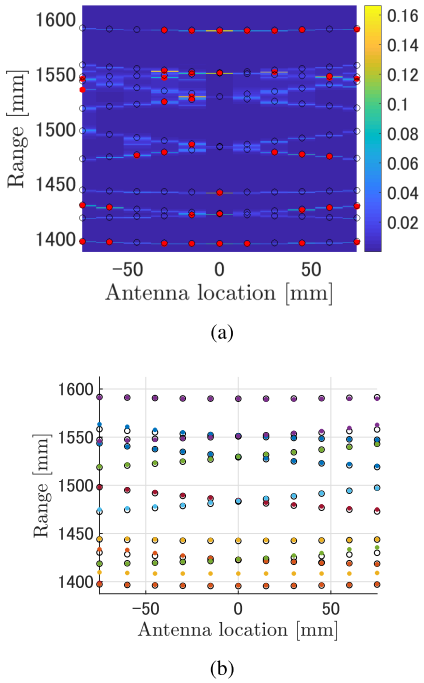

Fig. 21. Results of RP extractions in a 3-D model without noise. (a) Capon. (b) Proposed. Black hollow circles denote the true RPs, red solid circles in (a) denote the extracted RPs by Capon, and colored solid circles in (b) denote the extracted RPs by the proposed method, where each color denotes each cluster. Color scale in (a) denotes the magnitude of the Capon response.

We assume a simple human body model, which is expressed as an aggregation of 11 ellipsoids corresponding to the head, upper and lower torsos, arms, and legs, as shown in Fig. 19. This simplified target model enables us to assess the imaging accuracy more reliably and quantitatively. The transmitting signal forms a pulse-modulated signal, with a center frequency of 20 GHz and a bandwidth of 3.0 GHz, where the center wavelength and theoretical range resolutions are 15 and 50 mm, respectively. The 2-D (11 × 17) array with 7.5-mm (a half of center wavelength) equal spacing is located on the $y = 0$ plane, which consists of 11 antennas along the x-axis and 17 antennas along the z-axis. The received data are generated by GO, that is, the interferences among a number of reflections from multiple objects are considered in generating data.

2) Results: First, we will discuss the noise-free case. Fig. 21 shows the range extraction results obtained by the Capon and the proposed method. Note that, to suppress the sidelobe effect, the window function in the 2-D k-space is the raised cosine function with the width along the k_x axis of 0.775 rad/m and the width along the k_z axis of 1.21 rad/m, which almost corresponds to a size of spatial resolution in k-space. As shown in this figure, a number of reflection RPs are included in one range resolution (50 mm); then, a super-resolution technique, such as the Capon method, must be implemented. Since we assumed 11 ellipsoid targets, it is expected that each antenna will receive at least 11 RPs; however, the Capon method could not obtain a sufficient number of RPs at each location (ideally 11 points) because of its insufficient range resolution, that is, the Capon method has missed a significant RP for the

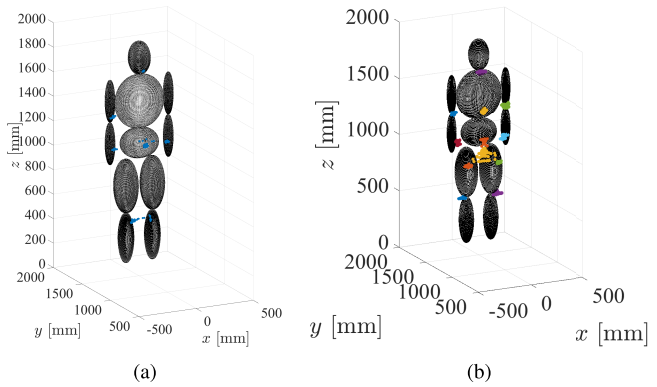

Fig. 22. Results of RPM imaging in a 3-D model without noise. (a) Capon. (b) Proposed. Red solid circles in (a) denote the reconstructed scattering center points by Capon via RPM. Colored solid circles in (b) denote the reconstructed scattering center points by the proposed method via RPM, where each color denotes each cluster.

RPM imaging. In contrast, the proposed method obtained over ten RPs with high accuracy by resolving the RPs using k-space decomposition. The number of RPs that satisfies $e \leq 10$ mm criterion is 678 for the Capon method (cumulative probability: 100 %) and 2248 for the proposed method (cumulative probability: 98 %). Note that the actual total number of RPs and scattering points is 2057 in this case. These results demonstrate that the proposed method remarkably enhances the number of RPs with high accuracy, which is much closer to the ideal number (2057). Finally, Fig. 22 shows the reconstruction results obtained by the RPM method, using the Capon method and the proposed range decomposition. By increasing the number of accurate RPs, the accuracy and imaging area of the RPM images are also enhanced. The 3-D image of the RPM offers a limited area of each ellipsoidal, and this is because each ellipsoid object has a smooth surface, and its surface specular reflection is dominant for each received signal $s(X, Z, R)$. However, the literature [17] demonstrated that the RPM offers a more informative image assuming an elaborate target, such as a realistic human body, even in using the Capon method. Then, if more accurate range estimation is achieved by the proposed method, it is well expected that its RPM image could express a larger area of a human body, namely, a more informative image, even using a lower fractional bandwidth radar system. The time required for computation by RPM with the Capon filter and the proposed method is 3.4×10^4 s and 20 s, respectively, on a computer with an Intel Xeon E5-2680 v4 2.40-GHz CPU and 128-GB RAM. The proposed method requires a remarkably shorter computational time because it offers RP clustering through k-space decomposition, which reduces the number of RPs input into the RPM. Note that, if more acceleration is needed, one could implement the extended algorithm in [17]. In addition, we compared the performance of the proposed method with that of the SAR imaging approach. Fig. 23 shows an image of the SAR, where the BP algorithm was applied to complex received data after matched filtering. The figure shows that, while SAR imaging could separate the three target responses along the azimuth direction, it offers considerably blurred images along the range direction because of the lower range resolution. Furthermore,

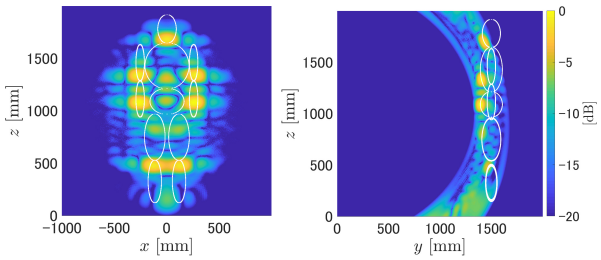

Fig. 23. Reconstruction images by the SAR method without noise. (a) Cross-sectional image at $y = 1000$ mm. (b) Cross-sectional image at $x = 0$ mm.

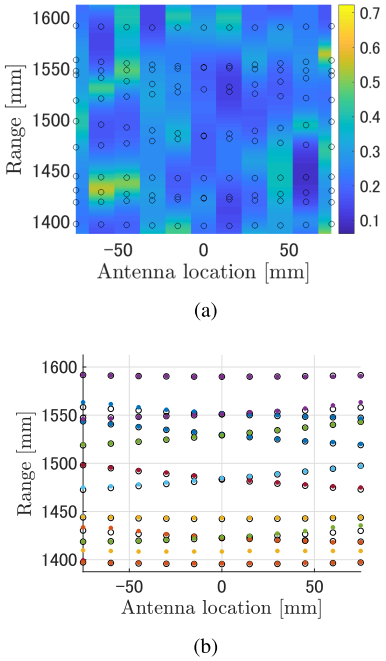

Fig. 24. Results of RP extractions in the 3-D model at $S/N = 20$ dB. (a) Capon. (b) Proposed. Black hollow circles denote the true RPs, and red solid circles in (a) denote the extracted RPs by Capon. Colored solid circles in (b) denote the extracted RPs by the proposed method, where each color denotes each cluster. Color scale in (a) denotes the magnitude of the Capon response.

even if we implemented the matrix operation-based acceleration scheme, the computational time required to run the DAS imaging algorithm is 180 s to obtain one cross-sectional image with a 3-mm pixel using the same processor described before. Also note that, in DAS image processing, computation time could be further reduced. If sufficient RAM is available and the region of interest and element positions are invariant in the sequential measurement, the computation could be reduced by separating the computation of the image area restoration, including the transfer function from each pixel and element, andmatrix multiplication with updated measured data. We have confirmed that, using the same processor and amount of RAM, the computation time required to obtain a single cross-sectional image (Fig. 23) can be reduced to approximately 18 s by applying the abovementioned separation process. However, we also confirmed that applying the

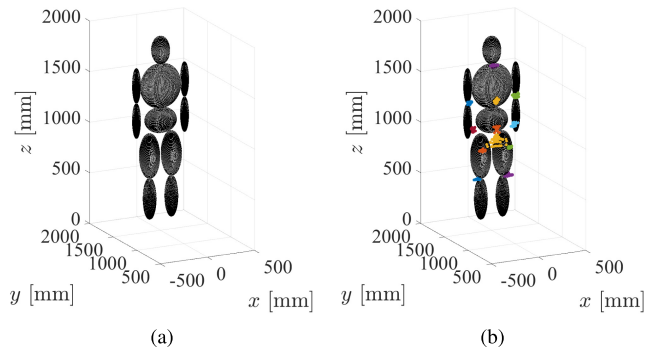

Fig. 25. Results of RPM imaging in the 3-D model at $S/N = 20$ dB. (a) Capon. (b) Proposed. Red solid circles in (a) denote the reconstructed scattering center points by Capon via RPM. Colored solid circles in (b) denote the reconstructed scattering center points by the proposed method via RPM, where each color denotes each cluster.

TABLE IV
CUMULATIVE PROBABILITY FOR RPM IMAGING ERRORS IN 3-D CASE

	$\mathrm{Err}_{\mathrm{Range}} \leq 10$ mm	
	S/N=∞ dB	S/N= 20 dB
Capon	100 % (678/678)	2.6 % (16/609)
Proposed	98 % (2248/2296)	98 % (2253/2298)

abovementioned approach to obtain the full 3-D volumetric image is not efficient because it consumes an excessive amount of RAM. For example, for a region of interest of -1000 mm $\leq x \leq 1000$ mm, 0 mm $\leq y \leq 2000$ mm, 0 mm $\leq z \leq 2000$ mm with 3-mm spacing, more than 128-GB RAM is required. In addition, if we do not apply the abovementioned process, it has been also confirmed that the total computation time required to obtain the abovementioned volumetric image is more than 1.2×10^5 s, which is much longer than the amount of time required by the proposed method.

3) Impact of Noise: Next, we assessed the noise robustness of each method by investigating their performance on data with additive noise, in which the Gaussian white noise was added to the received signal as $s(X, Z, R)$. Similar to the 2-D model, we investigated a mean S/N ratio of 20 dB. Fig. 24 shows the RP extraction results obtained using the Capon and the proposed method. While the proposed method maintains almost the same results as the noiseless case, the Capon method seriously suffers from inaccuracies in range extraction because of the additive noise. Consequently, the final reconstructed images obtained by RPM indicated that Capon-based range extraction could not offer a meaningful image, whereas the proposed method provides almost the same results as in the noiseless case, as shown in Fig. 25, namely, the proposed method has a significant advantage for the noise-robust feature. Finally, Tables IV and V summarize the quantitative results for the noise-free and noisy situations in terms of the errors obtained by each method for range extraction and RPM imaging results. It can be concluded from the abovementioned results that the proposed method maintains remarkable noise robustness compared with the Capon method because it

TABLE V
CUMULATIVE PROBABILITY FOR RPM IMAGING ERRORS IN 3-D CASE

	$\mathrm{Err}_{\mathrm{RPM}} \leq 50$ mm	
	S/N=∞ dB	S/N= 20 dB
Capon	99 % (341/344)	0 % (0/16)
Proposed	95 % (1155/1222)	95 % (1170/1237)

coherently integrates the received data along with the sensor locations, which significantly suppresses the random noise component.

VII. CONCLUSION

In this article, we introduced a new *k*-space decomposition preprocessing method for highly accurate RPM imaging for MMW short-range radar systems. The proposed method has numerous advantages, including higher azimuth and range resolutions and noise robustness, achieved through coherent preprocessing. In addition, the method offers prior RP clustering, which enhances the accuracy and processing speed of RPM imaging. We demonstrated through 2-D and experimental validations via an X-band radar system that the proposed method maintains highly accurate range measurements compared with the already existing Capon technique, which is much sensitive to additive noise. Finally, a 3-D observation model, which represents a simplified human body detection scenario, showed that the proposed method offers high-accuracy imaging results, even under severe conditions, such as narrowband scenarios.

The real contribution of the proposed method is that it could eliminate the shortcomings in both coherent and incoherent imaging approaches. The proposed method avoids ambiguous responses due to sparsely sampled data in the coherent imaging scheme because the imaging procedure itself is based on the incoherent process via the RPM algorithm. Furthermore, by introducing the k-space decomposition scheme, the proposed method could resolve the problem in the incoherent RPM process that it requires wider frequency bandwidth and does not obtain the advantage of the higher frequency radar system regarding azimuth resolution. It should be also noted that, while the *k*-space decomposition is implemented via the FFT scheme, the proposed method could avoid the far-field approximation (planar incident wave) error or ambiguous response. This is because the incoherent conversion from RP to its associated scattering center point assumes a near-field imaging scenario, which is free from the ambiguity due to phase uncertainty. Note that, while there is a possibility for generating a more accurate image by combining the Capon and the *k*-space decomposition in the RPM scheme, the accuracy for range estimation by the Capon highly depends on the SNR level, and the balance between accuracy and noise–robustness should be considered in regard to the practical situation.

Finally, we should mention the limitations of this method in considering realistic scenarios. First, the RPM imaging scheme relies on the geometric optics approximation to determine the dominant scattering center point on the target boundary using the discrete RPs data, namely, the roughness of the target surface should be much greater than the system center wavelength. Nonetheless, many studies have described its relevance and limitations, such as assuming a realistic human body case in [17]. Second, our proposed method does not consider the multiple reflection components, which would generate a ghost image, because the *k*-space data include some responses from multiple reflections, and we do not apply any suppression method here. These problems are common in other imaging schemes, such as SAR, RMA, or RPM, and are far beyond the topic under investigation in this study. Some promising solutions to deal with the multiple scattering components do exist, such as [24], [25], where the ghost images of multiple reflections are converted to real images using appropriate processing. However, those algorithms would incur more computational complexity, and it is our future task to incorporate these algorithms with less complexity.

REFERENCES

[1] J. A. Nanzer and R. L. Rogers, "Human presence detection using millimeter-wave radiometry," *IEEE Trans. Microw. Theory Techn.*, vol. 55, no. 12, pp. 2727–2734, Dec. 2007.
[2] M. Vahidpour and K. Sarabandi, "Millimeter-wave Doppler spectrum and polarimetric response of walking bodies," *IEEE Trans. Geosci. Remote Sens.*, vol. 50, no. 7, pp. 2866–2881, Jul. 2012.
[3] D. A. Andrews, S. W. Harmer, N. J. Bowring, N. D. Rezgui, and M. J. Southgate, "Active millimeter wave sensor for standoff concealed threat detection," *IEEE Sensors J.*, vol. 13, no. 12, pp. 4948–4955, Dec. 2013.
[4] B. Gonzalez-Valdes, Y. Alvarez, S. Mantzavinos, C. M. Rappaport, F. Las-Heras, and J. A. Martinez-Lorenzo, "Improving security screening: A comparison of multistatic radar configurations for human body imaging," *IEEE Antennas Propag. Mag.*, vol. 58, no. 4, pp. 35–47, Aug. 2016.
[5] B. D. Van Veen and K. M. Buckley, "Beamforming: A versatile approach to spatial filtering," *IEEE ASSP Mag.*, vol. 5, no. 2, pp. 4–24, Apr. 1988.
[6] F. Soldovieri, A. Brancaccio, G. Prisco, G. Leone, and R. Pierri, "A kirchhoff-based shape reconstruction algorithm for the multimonostatic configuration: The realistic case of buried pipes," *IEEE Trans. Geosci. Remote Sens.*, vol. 46, no. 10, pp. 3031–3038, Oct. 2008.
[7] J. M. Lopez-Sahcnez and J. Fortuny-Guasch, "3-D radar imaging using range migration techniques," *IEEE Trans. Antennas Propag.*, vol. 48, no. 5, pp. 728–737, May 2000.
[8] Z. Wang, Q. Guo, X. Tian, T. Chang, and H.-L. Cui, "Near-field 3-D millimeter-wave imaging using MIMO RMA with range compensation," *IEEE Trans. Microw. Theory Techn.*, vol. 67, no. 3, pp. 1157–1166, Mar. 2019.
[9] S. S. Ram and A. Majumdar, "High-resolution radar imaging of moving humans using Doppler processing and compressed sensing," *IEEE Trans. Aerosp. Electron. Syst.*, vol. 51, no. 2, pp. 1279–1287, Apr. 2015.
[10] F. Ahmad and M. G. Amin, "Through-the-wall human motion indication using sparsity-driven change detection," *IEEE Trans. Geosci. Remote Sens.*, vol. 51, no. 2, pp. 881–890, Feb. 2013.
[11] X. Zhuge and A. G. Yarovoy, "A sparse aperture MIMO-SAR-based UWB imaging system for concealed weapon detection," *IEEE Trans. Geosci. Remote Sens.*, vol. 49, no. 1, pp. 509–518, Jan. 2011.
[12] S. Kidera, T. Sakamoto, and T. Sato, "Accurate UWB radar three-dimensional imaging algorithm for a complex boundary without range point connections," *IEEE Trans. Geosci. Remote Sens.*, vol. 48, no. 4, pp. 1993–2004, Apr. 2010.
[13] T. Sakamoto, T. Sato, P. Aubry, and A. Yarovoy, "Fast imaging method for security systems using ultrawideband radar," *IEEE Trans. Aerosp. Electron. Syst.*, vol. 52, no. 2, pp. 658–670, Apr. 2016.
[14] Y. Sasaki, F. Shang, S. Kidera, T. Kirimoto, K. Saho, and T. Sato, "Three-dimensional imaging method incorporating range points migration and Doppler velocity estimation for UWB millimeter-wave radar," *IEEE Geosci. Remote Sens. Lett.*, vol. 14, no. 1, pp. 122–126, Jan. 2017.
[15] S. Kidera, T. Sakamoto, and T. Sato, "High-resolution and real-time three-dimensional imaging algorithm with envelopes of spheres for UWB radars," *IEEE Trans. Geosci. Remote Sens.*, vol. 46, no. 11, pp. 3503–3513, Nov. 2008.

[16] S. Takahashi and S. Kidera, "Acceleration of range points migration based microwave imaging for non-destructive testing," *IEEE Antennas Wireless Propag. Lett.*, vol. 17, no. 4, pp. 702–705, Apr. 2018.
[17] Y. Akiyama and S. Kidera, "Low complexity algorithm for range-point migration-based human body imaging for multistatic UWB radars," *IEEE Geosci. Remote Sens. Lett.*, vol. 16, no. 2, pp. 216–220, Feb. 2019.
[18] S. Kidera, T. Sakamoto, and T. Sato, "Super-resolution UWB radar imaging algorithm based on extended capon with reference signal optimization," *IEEE Trans. Antennas Propag.*, vol. 59, no. 5, pp. 1606–1615, May 2011.
[19] T. Hayashi and S. Kidera, "Incorporation of super-resolution Doppler analysis and compressed sensisng filter for UWB human body imaging radar," in *Proc. ISAP*, Oct. 2018, pp. 1–2.
[20] R. H. Stolt, "Migration by Fourier transform," *Geophysics*, vol. 43, no. 1, pp. 23–48, Feb. 1978.
[21] Y. Akiyama and S. Kidera, "*k*-space decomposition based range points migration method for millimeter wave radar," in *Proc. Int. Geosci. Remote Sens. Symp.*, Jul. 2019, pp. 680–683.
[22] V. U. Zavorotny and A. G. Voronovich, "Comparison of geometric optics and diffraction effects in radar scattering from steep and breaking waves," in *Proc. IEEE Int. Geosci. Remote Sens. Symp.*, Jul. 2007, pp. 1350–1353.
[23] J. Capon, "High-resolution frequency-wavenumber spectrum analysis," *Proc. IEEE*, vol. 57, no. 8, pp. 1408–1418, Aug. 1969.
[24] S. Kidera, T. Sakamoto, and T. Sato, "Extended imaging algorithm based on aperture synthesis with double-scattered waves for UWB radars," *IEEE Trans. Geosci. Remote Sens.*, vol. 49, no. 12, pp. 5128–5139, Dec. 2011.
[25] S. Kidera and T. Kirimoto, "Fast and shadow region 3-dimensional imaging algorithm with range derivative of doubly scattered signals for UWB radars," *IEEE Trans. Antennas Propag.*, vol. 60, no. 2, pp. 984–996, Feb. 2012.

Yoshiki Akiyama received the B.E. degree in electrical and electronic engineering and the M.E. degree in informatics and communication engineering from the University of Electro-Communications, Tokyo, Japan, in 2017 and 2019, respectively.

He joined Fujitsu Limited, Kawasaki, Japan, in 2019.

Tomoki Ohmori received the B.E. degree in communication engineering and informatics from the University of Electro-Communications, Tokyo, Japan, in 2019, where he is pursuing the M.E. degree with the Graduate School of Informatics and Engineering.

His research interest includes signal processing and imaging for microwave radar as well as its applications.

Shouhei Kidera (Member, IEEE) received the B.E. degree in electrical and electronic engineering and the M.I. and Ph.D. degrees in informatics from Kyoto University, Kyoto, Japan, in 2003, 2005, and 2007, respectively.

He has been with the Graduate School of Informatics and Engineering, University of Electro-Communications, Tokyo, since 2009, where he is an Associate Professor. He has been stayed at the Cross-Disciplinary Electromagnetics Laboratory, University of Wisconsin Madison, Madison, WI, USA, as the Visiting Researcher, in 2016. He has been a Principal Investigator of the PRESTO Program of Japan Science and Technology Agency (JST) from 2017 to 2021. His research interest is in advanced radar signal processing or electromagnetic inverse scattering issue for ultrawideband (UWB) 3-D sensor or biomedical applications.

Dr. Kidera is a member of the Institute of Electronics, Information, and Communication Engineers of Japan (IEICE), the Institute of Electrical Engineering of Japan (IEEJ), and the Japan Society of Applied Physics (JSAP). He was a recipient of the 2012 Ando Incentive Prize for the Study of Electronics, the 2013 Young Scientist's Prize by the Japanese Minister of Education, Culture, Sports, Science and Technology (MEXT), and the 2014 Funai Achievement Award.